frontiers in Materials

ORIGINAL RESEARCH
published: 27 March 2020
doi: 10.3389/fmats.2020.00070

Check for updates

Effect of Temperature on the Mechanical Properties and Deformation Mechanism of a High Mn Steel With Composite Structure

Xiaoman Chen[1,2], Yuhui Wang[1,2,3], Jianchao Xiong[1,2], Guoyang Li[1,2], Yanzhong Tian[4], Wenquan Cao[5] and Tiansheng Wang[1,2]**

[1] State Key Laboratory of Metastable Materials Science and Technology, Yanshan University, Qinhuangdao, China, [2] National Engineering Research Center for Equipment and Technology of Cold Strip Rolling, Yanshan University, Qinhuangdao, China, [3] Research Center for Light and High-Performance Materials, Nanjing Tech University, Nanjing, China, [4] Key Laboratory for Anisotropy and Texture of Materials (Ministry of Education), School of Materials Science and Engineering, Northeastern University, Shenyang, China, [5] Special Steel Department Central Iron and Steel Institute, Beijing, China

OPEN ACCESS

Edited by:
Zuhua Zhang,
Hunan University, China

Reviewed by:
Liangfeng Li,
Southwest University of Science and Technology, China
Jianxin Xie,
University of Science and Technology Beijing, China

***Correspondence:**
Yuhui Wang
yhwang@ysu.edu.cn
Tiansheng Wang
tswang@ysu.edu.cn

Specialty section:
This article was submitted to Structural Materials, a section of the journal Frontiers in Materials

Received: 22 January 2020
Accepted: 05 March 2020
Published: 27 March 2020

Citation:
Chen X, Wang Y, Xiong J, Li G, Tian Y, Cao W and Wang T (2020) Effect of Temperature on the Mechanical Properties and Deformation Mechanism of a High Mn Steel With Composite Structure. Front. Mater. 7:70. doi: 10.3389/fmats.2020.00070

A composite high manganese structure comprising recovered and recrystallized structures was prepared using a single-phase austenitic Fe-30Mn-0.14C-7Cr-0.26Ni steel by cold rolling and annealing. The yield strength and elongation of the composite increased simultaneously, when the tensile temperature decreased from room temperature (RT) to low temperature (−180°C). The composite structure exhibited a good combination of strength and ductility at RT and −180°C. The notable mechanical properties at low temperature can be attributed to the enhanced strain-hardening capability via introducing multiple deformation mechanisms in the composite structure.

Keywords: high manganese steel, composite structure, strength, cold rolling, annealing

INTRODUCTION

Fe–Mn alloys have attracted significant attention owing to their excellent mechanical properties such as the combination of high strength and high elongation as well as excellent work hardening ability (Bouaziz et al., 2011; Seol et al., 2013; Ueji et al., 2013; Shterner et al., 2016; Ghasri-Khouzani and McDermid, 2017; Wang et al., 2018a,b; Lee et al., 2019). These alloys have been widely reported as potentially low-temperature steels (Hong and Han, 1995; Wang et al., 2018a,b; Lee et al., 2019). The corresponding mechanical properties and deformation mechanism depend on the types of elements added in the alloy as well as on the deformation temperature (Grässel et al., 2000; Allain et al., 2004b; Wang et al., 2010; Lee et al., 2017).

The refined structure could increase the yield strength; however, the elongation may decrease (Huang et al., 2006; Wang et al., 2018b). Some effective methods could improve the strength and ductility of high manganese steels by tailoring the microstructure. As an example, the composite structure of layers of the recovered and recrystallized structures should be proposed. Wang et al. (2018b) used cold rolling and annealing to design Fe-34.5Mn-0.04C steel to form a composite structure comprising recovered and recrystallized structures, the resulting steel demonstrated a good combination of strength and ductility, along with good work hardening ability. Wu et al. (2015) reported that the lamellar structure of pure titanium would lead to the same strength as that of the fine-grained structure, as well as to the same elongation as the coarse-grained structure. Similarly, the IF steel, as reported by Zhang et al. (2017), would also demonstrate good mechanical properties attributing to the lamellar structure. In previous reports (Koyama et al., 2011; Gutierrez-Urrutia and Raabe, 2012; Renard and Jacques, 2012; Shterner et al., 2014, 2016), the formation of deformed twins could inhibit the movement of dislocations, as well as reduce the average free path of dislocations, while producing a dynamic Hall–Petch effect (Grässel et al., 2000; Karaman et al., 2000; Bouaziz and Guelton, 2001; Allain et al., 2004a); therefore, TWIP effect significantly improved the comprehensive mechanical properties. Consequently, the work hardening ability of high manganese steel would be improved (Shterner et al., 2016).

In this study, a high manganese (high-Mn) composite structure comprising recovered and recrystallized structures was successfully produced by cold rolling and annealing in using Fe-30Mn-0.14C-7Cr-0.26Ni steel as the substrate. The composite structure demonstrated a good combination of strength and ductility at room- and low- temperature. The deformation mechanism of the composite structure was also investigated in this study. Furthermore, the Hall–Petch relationship of the composite structure was compared to that of the cold-rolled structure, revealing single recovered structure and recrystallized equiaxed grain structure.

EXPERIMENTAL

Fe-30Mn-0.14C-7Cr-0.26Ni (wt. %) steel was used the substrate in this study. The steel was melted using a vacuum induction technique. **Table 1** shows the chemical composition of the high-Mn steel. The ingot was heated to 1,200°C and held for 4 h, and then forged to produce a 22 mm thick plate. The hot rolled temperature was >900°C. The plate was cold rolled with a thickness reduction of 95% using a laboratory rolling mill with a roll diameter of 230 mm, and a rotating speed of 35 r/min. This steel had good cold rolling deformation ability, and the cracks at the edges were not present during cold rolling. The sheet was annealed at 500, 600, 700, and 800°C for 1 h, at 900°C for 1, 2, and 3 h, as well as at 950°C for 1 h, and 1,000°C for 1 h to obtain various grain sizes. The grain size was determined by the intercept method.

The tensile tests were carried out using an MTS tensile machine equipped with a cryogenic chamber. The tensile direction was parallel to the rolling direction (RD) and the test was carried out at an initial rate of 10^{-3} s^{-1} at RT and −180°C. The gauge length and width of the tensile samples were 10 and 2 mm, respectively, at RT. The gauge length and width of the tensile samples were 50 and 12.5 mm at −180°C, respectively.

The XRD analysis of the cold-rolled sample was carried out using a D/max 2400 diffractometer equipped with Cu Kα radiation. The working voltage was 40 kV, and the working current was 200 mA. The microstructure of the composite was characterized by field-emission scanning electron microscopy (FE-SEM, FEI Talos 200X TEM) equipped with a backscattered electron (BSE) detector and an electron backscatter diffraction (EBSD) system were. The samples of SEM and EBSD were ground down to a few grits and mechanically polished. Finally, the surface stress was removed using a JEOL section polishing instrument at a voltage of 8 kV and the duration of 10 min. The EBSD working voltage was 20 kV, and the current was 6.4 nA. The OIM analysis data processing software was utilized for both processing and analysis. The TEM samples were ground down to 30 μm with different sandpapers and consequently prepared through twin-jet technique. The twin-jet technique solution comprised 10% perchloric acid and 90% alcohol. All the observed sections in these experiments were the RD-ND sections.

TABLE 1 | Chemical composition of the steel substrate (wt. %).

Mn	C	Cr	Ni	Fe
30	0.14	7	0.26	Bal.

RESULTS AND DISCUSSION

The Effect of Annealing on the Microstructure

Figure 1 shows the XRD patterns of the 95% cold-rolled sample, and martensitic diffraction peaks were not observed in the investigated steel. Therefore, all the samples in these experiments are single-phase austenite. **Figure 1** shows very weak γ(200) diffraction peak and very strong γ (111) and γ (220) peaks, indicating that texture evolved during 95% cold rolling.

Figure 2 shows the microstructure of lamellar samples. **Figure 2A** shows the electron channeling contrast image (ECCI) image of the cold rolled sample to 95%. The microstructure mainly composed of deformed twins (DT) (**Figure 2B**) and shear bands (SB), while the dislocation interface (**Figure 2C**) comprised low angle grain boundaries (LAGBs). The deformed twins accounted for ∼3%, and the average lamellar spacing was 13 nm. The recovered structures accounted for ∼97%, and the average lamellar spacing was 31 nm. The mean grain

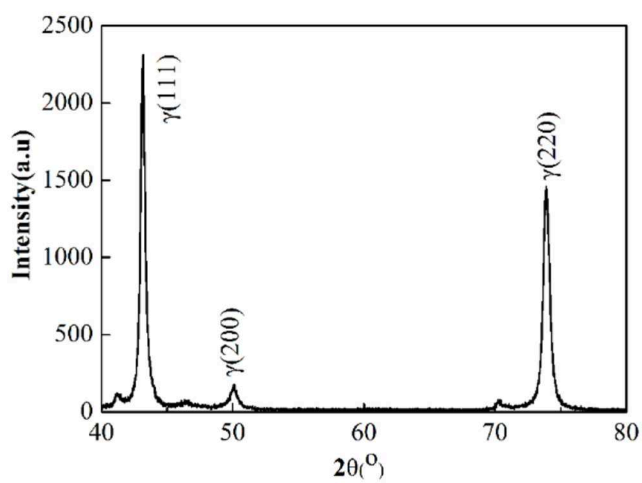

FIGURE 1 | X-ray patterns of the cold-rolled sample showing single-phase austenite.

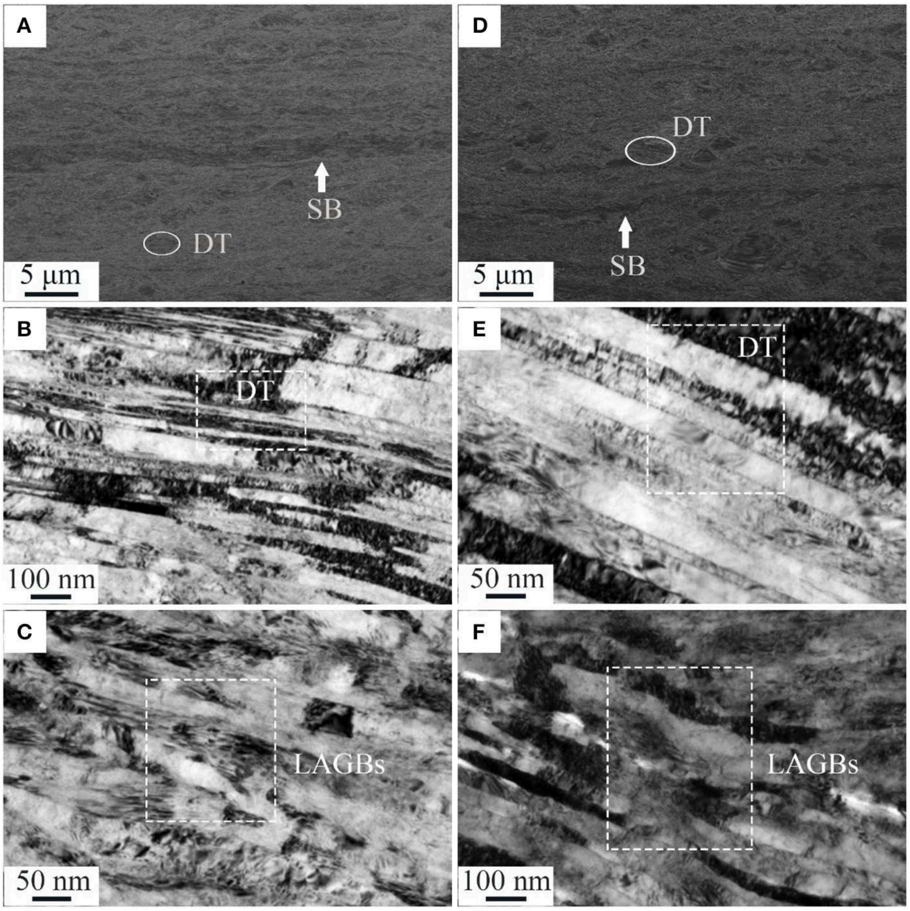

FIGURE 2 | Microstructures of lamellar samples. **(A)** ECCI image, **(B,C)** TEM images of the sample with the grain size of 0.03 μm; **(D)** ECCI image, **(E,F)** TEM images of the sample with the grain size 0.05 μm.

size (boundary spacing) was ∼0.03 μm. **Figure 2D** shows the ECCI image of the sample obtained by cold rolling to 95%, followed by annealing at 500°C for 1 h. This sample exhibited similar microstructure as that of the cold rolled sample to 95%, the microstructure composted of SB, DT (**Figure 2E**) and LAGBs (**Figure 2F**). The mean grain size (boundary spacing) was ∼0.05 μm.

Figure 3 shows the microstructure of cold rolled to 95% and subsequent annealing at 600°C for 1 h. The IPF image (**Figure 3A**) and IQ image (**Figure 3B**) show the formation of a composite structure comprising recovered and recrystallized structures. Moreover, a small number of deformed twins were observed (**Figures 3C,D**), accounting for ∼1.6% and the average lamellar spacing was 43.4 nm. The recovered structures accounted for ∼13.4% and the average lamellar spacing was 69 nm. The recrystallized structures accounted for ∼85%, and the average grain size was 0.74 μm. The mean grain size of the composite structure was 0.65 μm after calculating the weighted average of the recovered and recrystallized structures.

The precipitates began to appear within the grains of the samples (**Figure 3E**), and the corresponding SADPs (**Figure 3F**) indicated that the precipitate was $Cr_{23}C_6$ carbide.

Figure 4 shows the microstructure produced by cold rolling to 95%, followed by subsequent annealing at 900°C for 1 h. **Figure 4A** shows a recrystallized equiaxed grain structure containing annealed twins with increasing annealing temperature. The mean grain size was ∼5.75 μm. **Figure 4B** shows that with increasing annealing temperature, the carbide dissolved, and no carbide existed within the grains, and only a few dislocation lines were detected.

The Mechanical Properties at RT and −180°C

Figure 5 shows the tensile stress–strain curves and the corresponding work hardening curves of the samples with the grain size in the range 0.03–5.75 μm at RT. The tensile strength of the samples with the grain sizes of 0.03 and 0.05 μm were relatively high, 1607 and 1588 MPa, respectively, as shown in **Figure 5A**; the yield strengths were 1477 and 1446 MPa, respectively; however, the elongation was quite low as uniform elongation was 2.5 and 2.4%, respectively. The composite structure of the samples with the grain size 0.65 μm has a good combination of strength and ductility, with the tensile strength as 918 MPa and the yield strength as 857 MPa, while

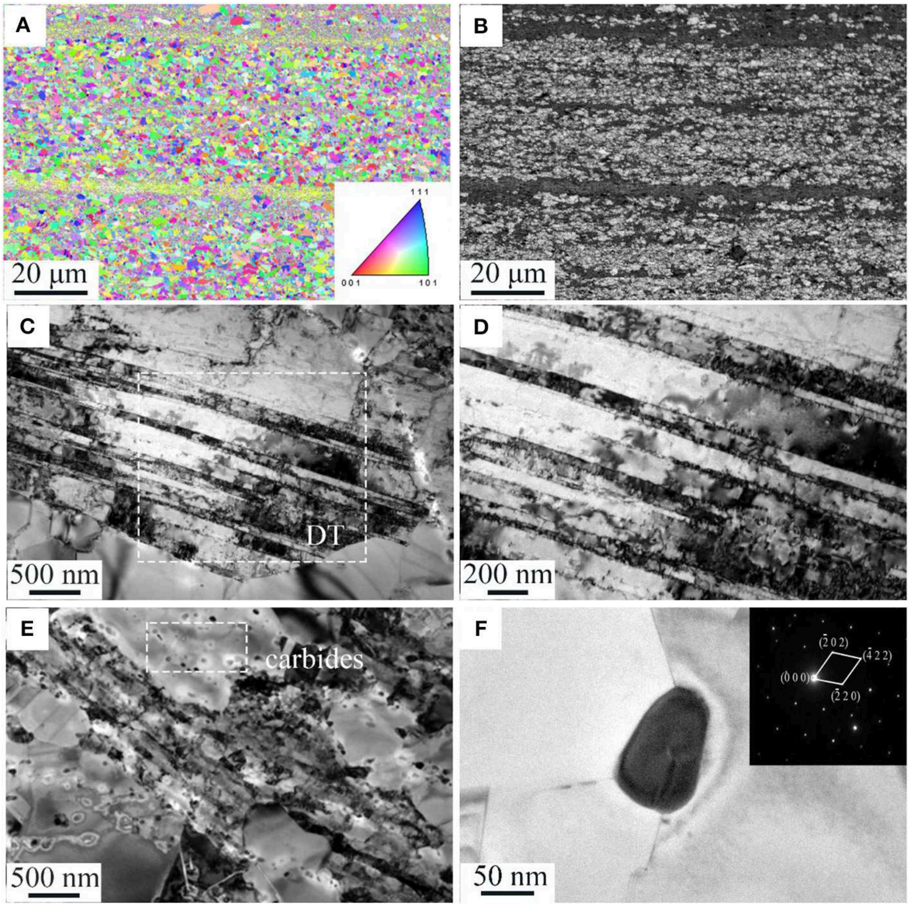

FIGURE 3 | Composite recovered and recrystallized structures. **(A)** IPF image, **(B)** IQ image, **(C)** TEM images, **(D)** a higher magnification of the region marked by white-dotted line in **(C)** show the deformed twins, **(E)** TEM image of carbides, and **(F)** a higher magnification with selected area diffraction patterns (SADPs).

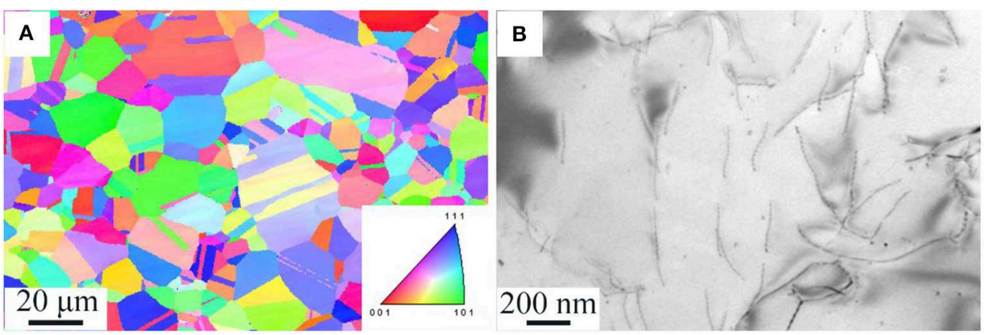

FIGURE 4 | Microstructure of the cold rolled sample to 95%, followed by subsequent annealing at 900°C for 1 h. **(A)** IPF image and **(B)** TEM image.

maintaining a good ductility. The uniform elongation was 14.7%, and the total elongation was 25.2%. The composite structure could be regarded as a special case of multiphase structure. The Hall–Petch relationship is described as follows:

$$\sigma_{YS}\,(MPa) = \sigma_0 + K_{YS} D^{\frac{-1}{2}} \quad (1)$$

where σ_{YS} is the yield stress, σ_0 is the resistance of the lattice to dislocation, K_{SY} is the grain boundary strengthening, and D is the grain size (Lee et al., 2019). It could be observed that the recovered structure as the hard phase and the recrystallized structure as the soft phase (Luo et al., 2019). The soft layer of the recrystallized grains began to plastically deform during tensile test; however, the plastic deformation would be limited by the surrounding hard layer to produce strengthening from a constraint effect (Wang et al., 2018c).

The curves show that the grain sizes had a significant effect on the tensile behavior. A discontinuous flow associated with a small Lüders elongation takes place in the sample with the grain size of 0.65 μm. The yield platform disappeared, and the tensile curves changed to continuous flow in the sample with the grain size of 5.75 μm.

The critical density of the motion dislocations required to initiate the plastic deformation increased with decreasing grain size, while the initial density of the motion dislocations was insufficient with the refinement of the grain size to submicron level, resulting in the yield platform appearance (Xie et al., 2019). The phenomenon of the yield platform was also reported for aluminum alloy (Wen and Morris, 2004; Nes et al., 2005; Nijs et al., 2008). In these reports, it was believed that the yield platform was caused by dislocation slip. A similar yield platform occurred in dual-phase high-Mn steel (Fu et al., 2012), caused by the martensitic transformation. Fe-Mn-C system steel also exhibited the phenomenon of yield platform. Similarly, the yield platform phenomenon in this experiment was found during the tensile testing of the pristine Ti sample (Li et al., 2013) and the fine-grained Fe-34.5Mn-0.04C steel (Wang et al., 2018b).

Figure 5B shows that the work hardening curves of samples with the grain sizes of 0.03 μm and 0.05 μm had only one stage. With increasing strain, the work hardening rapidly decreased, and the material formed bottlenecks quickly, and consequently fractured. The work hardening curve is divided into three stages for the samples with the grain size of 0.65 μm. In the first stage, the work hardening rate decreased rapidly with increasing strain, due to the lack of motion dislocation existence in the fine grain structure; in the second stage, with increasing strain, the work hardening rate increased, the deformed twins amount increased; in the third stage, as the strain continued to increase, the work hardening rate slightly fluctuated, but the general trend was slow decrease, due to the size reduction of the primary deformed twins (Misra et al., 2015). For the sample with the grain size of 5.75 μm, the work hardening curve could be divided into two stages: (i) the low strain stage, in which, the work hardening rate rapidly decreased with increasing strain due to the transformation of deformation mechanism from elastic to plastic, and (ii) the high strain stage, in which, the work hardening rate slowly decreased with increasing strain, while the material formed bottlenecks preceding fracture.

Figure 6 shows the tensile stress–strain curves and the corresponding work hardening curves at −180°C. **Figure 6A** shows that similar to the RT, the samples with the grain sizes

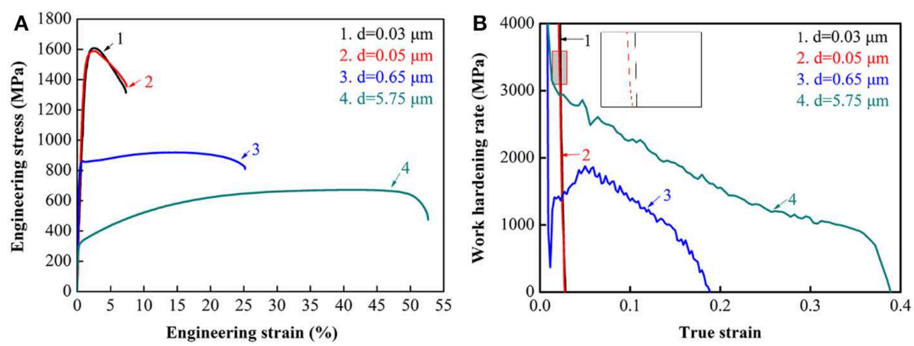

FIGURE 5 | Engineering stress–strain curves and corresponding work hardening curves of samples with different grain sizes at RT. **(A)** Engineering stress–strain curves and **(B)** work hardening curves.

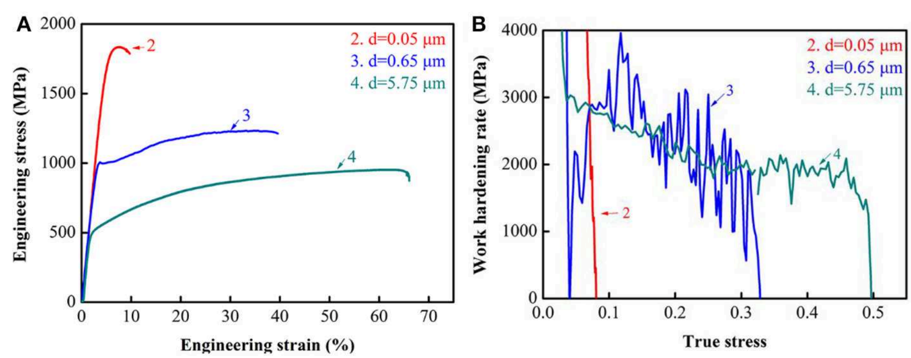

FIGURE 6 | Engineering stress–strain curves and corresponding work hardening curves of the samples with different grain sizes at −180°C. **(A)** Engineering stress–strain curves and **(B)** corresponding work hardening curves.

of 0.65 μm presented a yield platform with the tensile strength, yield strength, uniform elongation, and total elongation as 1231, 996 MPa, 37.0 and 42.0%, respectively. The samples with the grain size of 0.65 μm show a good combination of strength and ductility at low temperature. The tensile strength, yield strength, uniform elongation, and total elongation increased by 34.1, 16.2, 152.0, and 66.7%, respectively, compared to that at RT.

Figure 6B presents the work hardening curves of the samples with different grain sizes at low temperature. The work hardening curve of the sample with the grain size of 0.05 μm had only one stage. With increasing strain, the work hardening decreased rapidly and the material formed bottlenecks quickly, as well as fracture. The work hardening curve of the samples with the grain size of 0.65 μm can be divided into four stages: (i) in the first stage, with increasing strain, the work hardening rate rapidly decreased; (ii) in the second stage with increasing strain, the work hardening rate rapidly increased, as a result of the dislocation source strengthening; (iii) in the third stage, with increasing strain, the work hardening rate fluctuated slightly, but it remained stable as a whole; (iv) in the fourth stage, with further increase in the strain, the work hardening rate decreased sharply and fracture occurred. The work hardening curve of the sample with the size of 5.75 μm can be divided into three stages: (i) in the first stage, with increasing strain, the work hardening rate rapidly decreased, due to the transformation of deformation mechanism from elastic to plastic, (ii) in the second stage, with increasing strain, the work hardening rate slowly decreased, while in this stage, the coarse-grained structure deformed similar to the dislocation slip, and (iii) in the third stage, as the strain continued to increase, the work hardening rate remained unchanged.

The Relationship Between the Microstructure and Mechanical Properties

Figure 7 shows the EBSD maps of the specimens with the grain size of 0.65 and 5.75 μm after the tensile test. Limited by the resolution of EBSD maps, deformation twins were not observed in the recrystallized grain of the composite structure, as shown in **Figure 7A**; however, they were observed in the samples of the recrystallized equiaxed grain structure, as shown in **Figure 7C**. Martensitic transformation was not detected in these two type samples, as shown in **Figures 7B,D**.

To further understand the deformation mechanism of the sample with composite structure with the mean grain size of 0.65 μm, the specimens after the tensile tests were stretched to 1 and 3%, and their microstructures after deformation were observed by TEM. **Figures 8A,B** show the TEM images of the microstructures after deformation of the samples stretched to 1 and 3%, respectively. Different from the structures stretched to 1 and 3%, deformed twins appear in the recrystallized grains of the composite structure, demonstrating the formation of deformed twins in the composite structure at low strain.

The Evolution Mechanism of Hall–Petch Relationship

The tensile strength of the investigated steel annealed under different conditions was investigated in detail, as listed in **Table 2**. The corresponding Hall–Petch curves of the yield strength and the grain size are presented in **Figure 9**. The yield stress is a

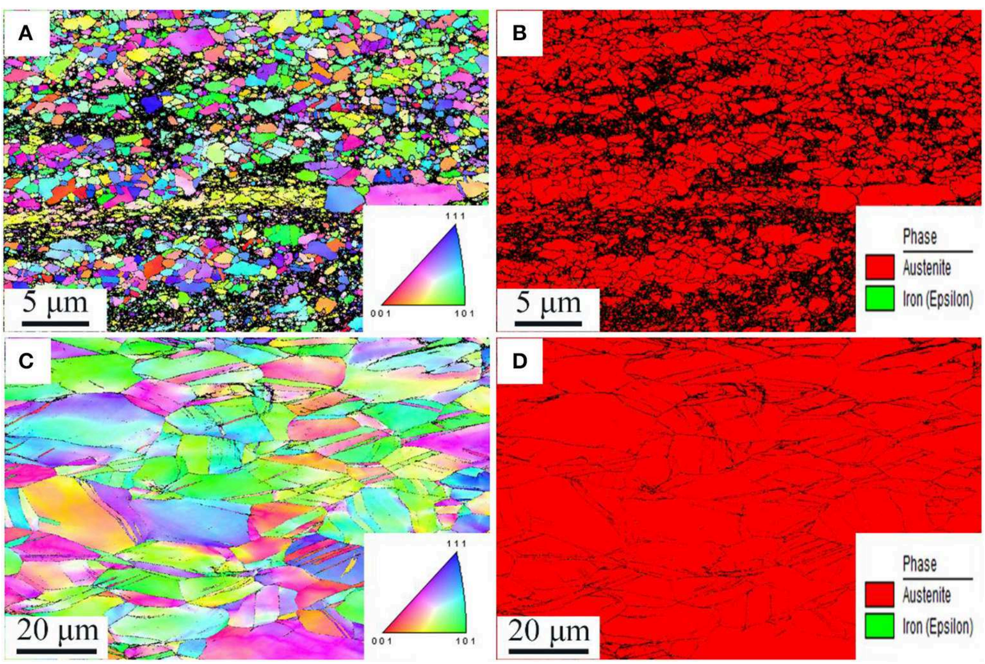

FIGURE 7 | EBSD images and phase images of samples with the grain sizes of 0.65 and 5.75 μm after the tensile tested. **(A)** IPF and **(B)** phase images of the sample with the grain size of 0.65 μm after the tensile test; **(C)** IPF and **(D)** phase images of the sample with the grain size of 5.75 μm after the tensile test.

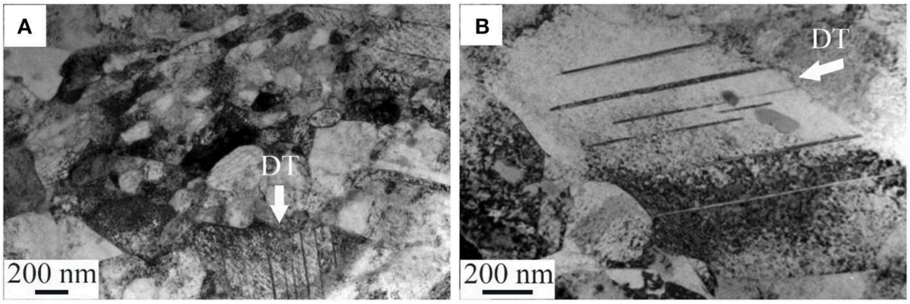

FIGURE 8 | TEM images of the microstructure of the samples with the grain size of 0.65 μm after the tensile test at **(A)** 1% and **(B)** 3%.

TABLE 2 | Microstructure, structural parameters, and yield strength of the investigated steel cold rolled to 95%, followed by annealing under different conditions.

Sample	Cold rolling and annealing	Microstructure	Yield strength (MPa)	Lamellar spacing/grain size (μm)
1	Cold-rolled to 95%	Lamellar structure	1,477	0.03 (Lamellar spacing)
2	500°C, 1 h	Lamellar structure	1,446	0.05 (Lamellar spacing)
3	600°C, 1 h	Composite structure Deformed twins (1.6%) Recovered (13.4%) Recrystallized (85%)	857	0.65
4	700°C 1 h	Equiaxed grains	679	0.80
5	800°C, 1 h	Equiaxed grains	535	1.07
6	900°C, 1 h	Equiaxed grains	322	5.75
7	900°C, 2 h	Equiaxed grains	266	11.00
8	900°C, 3 h	Equiaxed grains	247	12.60
9	950°C, 1 h	Equiaxed grains	266	13.50
10	1000°C, 1 h	Equiaxed grains	241	14.05

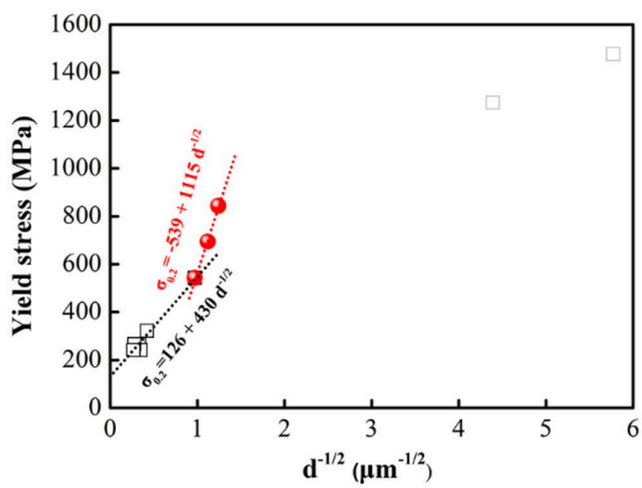

FIGURE 9 | Hall–Petch plot relationship at RT.

plot of a function of $d^{-1/2}$ in order to carry out the Hall–Petch analysis. Similar to the Hall–Petch curves of high-purity Al (Kamikawa et al., 2009) and Fe-34.5Mn-0.04C steel (Wang et al., 2018c), the k_y becomes significantly high in the fine grain size range (0.65 $\mu m \leq d \leq 1.07\ \mu m$) than that of the coarse-grained structure.

Deformed twins formed in the crystallization grains of composite structure and recrystallized equiaxed grain structure. The deformation mechanism of the composite mainly comprises deformed twin and dislocation slip. The deformed twins had a positive effect on the material properties. Deformed twins significantly improved the work hardening, because they could limit the dislocation slip (Gutierrez-Urrutia and Raabe, 2011, 2012; Renard and Jacques, 2012; Shterner et al., 2014), while reducing the mean free path of dislocations during strain processing and generating dynamic Hall–Petch effects (Grässel et al., 2000; Karaman et al., 2000; Bouaziz and Guelton, 2001; Allain et al., 2004a). The slope of the composite structure was significantly higher than that of other structures, caused by the composite structure interaction of the layers of the recovered and recrystallized structures during deformation, as well as pinned or blocked dislocations by the $Cr_{23}C_6$ carbide.

CONCLUSIONS

A composite material comprising recovered and recrystallized structures was prepared from Fe-30Mn-0.14C-7Cr-0.26Ni steel by cold rolling to 95%, followed by annealing at 600°C for 1 h. The yield strength and elongation of the composite structure were 857 MPa and 25.2% at RT, respectively, whereas 996 MPa and 42.0% at −180°C. Deformed twins formed in the recrystallized grains of the composite structure. The Hall–Petch slope k_y of the composite structure was higher than that of the coarse-grained structures. The composite structure showed multiple deformation mechanisms of dislocation and deformation twinning, enhancing the yield strength and ductility.

DATA AVAILABILITY STATEMENT

The datasets generated for this study are available on request to the corresponding author.

AUTHOR CONTRIBUTIONS

YW and TW designed the research and analyzed the data. YW and XC performed the research and analyzed the data and wrote the paper. JX, GL, YT, and WC contributed to the revisions.

FUNDING

This work was financially supported by the National Nature Science Foundation of China (Grant No. 51871194), the National Natural Foundation of Hebei Province, China (Grant No. E2018203312) and the Fundamental Research Funds for the Central Universities under Grant No. N180204015.

REFERENCES

Allain, S., Chateau, J. P., and Bouaziz, O. (2004a). A physical model of the twinning-induced plasticity effect in a high manganese austenitic steel. *Mater. Sci. Eng. A* 387–389, 143–147. doi: 10.1016/j.msea.2004.01.060

Allain, S., Chateau, J. P., Bouaziz, O., and Guelton, S. N. (2004b). Correlations between the calculated stacking fault energy and the plasticity mechanisms in Fe–Mn–C alloys. *Mater. Sci. Eng. A* 387–389, 158–162. doi: 10.1016/j.msea.2004.01.059

Bouaziz, O., Allain, S., Scott, C. P., Cugy, P., and Barbier, D. (2011). High manganese austenitic twinning induced plasticity steels: a review of the microstructure properties relationships. *Curr. Opin. Solid State Mater. Sci.* 15, 141–168. doi: 10.1016/j.cossms.2011.04.002

Bouaziz, O., and Guelton, N. (2001). Modelling of TWIP effect on work-hardening. *Mater. Sci. Eng. A* 319–321, 246–249. doi: 10.1016/S0921-5093(00)02019-0

Fu, L. M., Li, Z. M., Wang, H. N., Wang, W., and Shan, A. D. (2012). Lüders-like deformation induced by delta-ferrite-assisted martensitic transformation in a dual-phase high-manganese steel. *Scr. Mater.* 67, 297–300. doi: 10.1016/j.scriptamat.2012.05.010

Ghasri-Khouzani, M., and McDermid, J. R. (2017). Microstructural evolution and mechanical behaviour of Fe-30Mn-C steels with various carbon contents. *Mater. Sci. Technol.* 33, 1159–1170. doi: 10.1080/02670836.2016.1268662

Grässel, O., Krüger, L., Frommeyer, G., and Meyer, L. W. (2000). High strength Fe–Mn–(Al, Si) TRIP/TWIP steels development–properties–application. *Int. J. Plast.* 16, 1391–1409. doi: 10.1016/S0749-6419(00)00015-2

Gutierrez-Urrutia, I., and Raabe, D. (2011). Dislocation and twin substructure evolution during strain hardening of an Fe−22wt. % Mn−0.6wt. % C TWIP steel observed by electron channeling contrast imaging. *Acta Mater.* 59, 6449–6462. doi: 10.1016/j.actamat.2011.07.009

Gutierrez-Urrutia, I., and Raabe, D. (2012). Multistage strain hardening through dislocation substructure and twinning in a high strength and ductile weight-reduced Fe–Mn–Al–C steel. *Acta Mater.* 60, 5791–5802. doi: 10.1016/j.actamat.2012.07.018

Hong, S. H., and Han, Y. S. (1995). The effects of deformed twins and strain-induced ε-martensite on mechanical properties of an Fe-32Mn-12Cr-0.4C cryogenic alloy. *Scr. Metall. Mater.* 32, 489–1494. doi: 10.1016/0956-716X(95)00193-Y

Huang, X. X., Hansen, N., and Tsuji, N. (2006). Hardening by annealing and softening by deformation in nanostructured metals. *Science* 312, 249–251. doi: 10.1126/science.1124268

Kamikawa, N., Huang, X. X., Tsuji, N., and Hansen, N. (2009). Strengthening mechanisms in nanostructured high-purity aluminium deformed to high strain and annealing. *Acta Mater.* 57, 4198–4208. doi: 10.1016/j.actamat.2009.05.017

Karaman, I., Sehitoglu, H., Gall, K., Chumlyakov, Y. I., and Maier, H. J. (2000). Deformation of single crystal Hadfield steel by twinning and slip. *Acta Mater.* 48, 1345–1359. doi: 10.1016/S1359-6454(99)00383-3

Koyama, M., Sawaguchi, T., and Tsuzaki, K. (2011). Work hardening and uniform elongation of an ultrafine-grained Fe−33Mn binary alloy. *Mater. Sci. Eng. A* 530, 659–663. doi: 10.1016/j.msea.2011.10.038

Lee, S. I., Lee, S. Y., Han, J., and Hwang, B. (2019). Deformation behavior and tensile properties of an austenitic Fe-24Mn-4Cr-0.5C high-manganese steel: effect of grain size. *Mater. Sci. Eng. A* 742, 334–343. doi: 10.1016/j.msea.2018.10.107

Lee, S. J., Han, J., Lee, S., Kang, S. H., Lee, S. M., and Lee, Y. K. (2017). Design for Fe-high Mn alloy with an improved combination of strength and ductility. *Sci. Rep.* 7:3573. doi: 10.1038/s41598-017-03862-y

Li, Z. M., Fu, L. M., Fu, B., and Shan, A. D. (2013). Yield point elongation in fine-grained titanium. *Mater. Lett.* 96, 1–4. doi: 10.1016/j.matlet.2012.12.115

Luo, X., Huang, T. L., Wang, Y. H., Xin, Y. C., and Wu, G. L. (2019). Strong and ductile AZ31 Mg alloy with a layered bimodal structure. *Sci. Rep.* 9:5428. doi: 10.1038/s41598-019-41987-4

Misra, R. D. K., Challa, V. S. A., Venkatsurya, P. K. C., Shen, Y. F., and Somani, M. C., and Karjalainen, L. P. (2015). Interplay between grain structure, deformation mechanisms and austenite stability in phase-reversion-induced nanograined/ultrafine-grained austenitic ferrous alloy. *Acta Mater.* 84, 339–348. doi: 10.1016/j.actamat.2014.10.038

Nes, E., Holmedal, B., Evangelista, E., and Marthinsen, K. (2005). Modelling grain boundary strengthening in ultra-fine grained aluminum alloys. *Mater. Sci. Eng. A* 410–411, 178–182. doi: 10.1016/j.msea.2005.08.121

Nijs, O., Holmedal, B., Friis, J., and Nes, E. (2008). Sub-structure strengthening and work hardening of an ultra-fine grained aluminium–magnesium alloy. *Mater. Sci. Eng. A* 483–484, 51–53. doi: 10.1016/j.msea.2006.11.166

Renard, K., and Jacques, P. J. (2012). On the relationship between work hardening and twinning rate in TWIP steels. *Mater. Sci. Eng. A* 542, 8–14. doi: 10.1016/j.msea.2012.01.123

Seol, J. B., Jung, J. E., Jang, Y. W., and Park, C. G. (2013). Influence of carbon content on the microstructure, martensitic transformation and mechanical properties in austenite/ε-martensite dual-phase Fe–Mn–C steels. *Acta Mater.* 61, 558–578. doi: 10.1016/j.actamat.2012.09.078

Shterner, V., Timokhina, I. B., and Beladi, H. (2014). The correlation between stacking fault energy and the work hardening behaviour of high-Mn twinning induced plasticity steel tested at various temperatures. *Adv. Mater. Res.* 922, 676–681. doi: 10.4028/www.scientific.net/AMR.922.676

Shterner, V., Timokhina, I. B., and Beladi, H. (2016). On the work-hardening behaviour of a high manganese TWIP steel at different deformation temperatures. *Mater. Sci. Eng. A* 669, 437–446. doi: 10.1016/j.msea.2016.05.104

Ueji, R., Takagi, Y., Tsuchida, N., Shinagawa, K., Tanaka, Y., and Mizuguchi, T. (2013). Crystallographic orientation dependence of ε martensite transformation during tensile deformation of polycrystalline 30% Mn austenitic steel. *Mater. Sci. Eng. A* 576, 14–20. doi: 10.1016/j.msea.2013.03.071

Wang, X., Zurob, H. S., Embury, J. D., Ren, X., and Yakubtsov, I. (2010). Microstructural features controlling the deformation and recrystallization behaviour Fe−30%Mn and Fe−30%Mn−0.5%C. *Mater. Sci. Eng. A* 527, 3785–3791. doi: 10.1016/j.msea.2010.03.014

Wang, Y. H., Kang, J. M., Peng, Y., Wang, T. S., Hansen, N., and Huang, X. X. (2018b). Laminated Fe-34.5 Mn-0.04C composite with high strength and ductility. *J. Mater. Sci. Technol.* 34, 1939–1943. doi: 10.1016/j.jmst.2018.05.013

Wang, Y. H., Kang, J. M., Peng, Y., Wang, T. S., Hansen, N., and Huang, X. X. (2018c). Hall-Petch strengthening in Fe-34.5Mn-0.04C steel cold-rolled, partially recrystallized and fully recrystallized. *Scr. Mater.* 155, 41–45. doi: 10.1016/j.scriptamat.2018.06.019

Wang, Y. H., Shi, B. D., He, Y. M., Zhang, H. W., Peng, Y., and Wang, T. S. (2018a). A fine grain, high Mn steel with excellent cryogenic temperature properties and corresponding constitutive behaviour. *Materials* 11:E253. doi: 10.3390/ma11020253

Wen, W., and Morris, J. G. (2004). The effect of cold rolling and annealing on the serrated yielding phenomenon of AA5182 aluminum alloy. *Mater. Sci. Eng. A* 373, 204–216. doi: 10.1016/j.msea.2004.01.041

Wu, X. L., Yang, M. X., Yuan, F. P., Wu, G. L., Wei, Y. J., Huang, X. X., et al. (2015). Heterogeneous lamella structure unites ultrafine-grain strength with coarse-grain ductility. *Proc Natl Acad Sci U.S.A.* 112, 14501–14505. doi: 10.1073/pnas.1517193112

Xie, L., Wang, C. P., Wang, Y. H., Wu, G. L., and Huang, X. X. (2019). Grain size effect on the mechanical behavior of metastable Fe-23Cr-8.5Ni Alloy. *Metals* 9:734. doi: 10.3390/met9070734

Zhang, L., Chen, Z., Wang, Y. H., Ma, G. Q., Huang, T. L., Wu, G. L., et al. (2017). Fabricating interstitial-free steel with simultaneous high strength and good ductility with homogeneous layer and lamella structure. *Scr. Mater.* 141, 111–114. doi: 10.1016/j.scriptamat.2017.06.044

Conflict of Interest: The authors declare that the research was conducted in the absence of any commercial or financial relationships that could be construed as a potential conflict of interest.